PAPER

First-principles study of thermoelectric properties of Mg$_2$Si–Mg$_2$Pb semiconductor materials†

Tao Fan, [ID] *[ab] Congwei Xie,[ac] Shiyao Wang,[a] Artem R. Oganov*[acd] and Laifei Cheng[b]

Mg$_2$X^{IV} (X^{IV} = Si, Ge, Sn) compounds are semiconductors and their solid solutions are believed to be promising mid-temperature thermoelectric materials. By contrast, Mg$_2$Pb is a metal and few studies have been conducted to investigate the thermoelectric properties of Mg$_2$Si–Mg$_2$Pb solid solutions. Here, we present a theoretical study exploring whether Mg$_2$Pb–Mg$_2$Si solid solutions can be used as thermoelectric materials or not. We firstly constructed several Mg$_2$Si$_{1-x}$Pb$_x$ (0 ≤ x ≤ 1) structures and calculated their electronic structures. It is suggested that Mg$_2$Si$_{1-x}$Pb$_x$ are potential thermoelectric semiconductors in the range of 0 ≤ x ≤ 0.25. We then explicitly computed the electron relaxation time and both the electronic and lattice thermal conductivities of Mg$_2$Si$_{1-x}$Pb$_x$ (0 ≤ x ≤ 0.25) and studied the effect of Pb concentration on the Seebeck coefficient, electrical conductivity, thermal conductivity, and thermoelectric figure of merit (ZT). At low Pb concentration (x = 1/16), the ZT of the Mg$_2$Si$_{1-x}$Pb$_x$ solid solutions (up to 0.67 at 900 K) reaches a maximum and is much higher than that of Mg$_2$Si.

1 Introduction

Mg$_2$X^{IV} (X^{IV} = Si, Ge, Sn) compounds and their solid solutions are promising candidates as mid-temperature thermoelectric materials because of their relatively high figure of merit ZT, good mechanical strength and chemical stability, low cost, low density, and environmental friendliness.[1–6,53] A good thermoelectric material has a high figure of merit ZT, defined as, ZT = $\alpha^2 \sigma T/\kappa$, where α is the Seebeck coefficient, σ is the electrical conductivity, κ is the thermal conductivity, and T is the absolute temperature. To increase the ZT of Mg$_2$X^{IV} compounds and their solid solutions, many methods have been proposed over the last few decades, such as carrier doping,[7–12] nanostructuring,[13,14] electron-energy filtering,[15,16] band-structuring engineering,[17–19] and band convergence.[20–22]

With those great efforts, the ZT among Mg$_2$X^{IV} compounds and their solid solutions has been greatly improved.[21–27] Liu et al.[21] synthesized a series of Mg$_2$Si$_{1-x}$Sn$_x$ solid solutions (0.2 ≤ x ≤ 0.8) and measured their transport properties. Their first-principles calculation confirmed that two low-lying conduction bands of Mg$_2$Si$_{1-x}$Sn$_x$ coincide in energy at x ≈ 0.7. At this concentration, the Seebeck coefficient α of Mg$_2$Si$_{1-x}$Sn$_x$ is maximized and yields the highest ZT (1.3 around 700 K). Furthermore, they reported that the thermoelectric performance of Mg$_2$Sn$_{0.75}$Ge$_{0.25}$ can be better than that of Mg$_2$Si$_{0.3}$Sn$_{0.7}$. They found a similar band convergence in Mg$_2$Sn–Mg$_2$Ge solid solutions near the composition Mg$_2$Sn$_{0.75}$Ge$_{0.25}$ and the highest ZT for Mg$_2$Sn$_{0.75}$Ge$_{0.25}$ is 1.4 at 723 K.[24] Mao et al.[27] investigated the thermoelectric properties of Mg$_2$Sn–Mg$_2$Ge–Mg$_2$Si solid solutions. The maximum ZT among these solid solutions is about 1.3 at 723 K.

Recently, Muthiah et al.[28] experimentally investigated thermoelectric properties of Mg$_2$Si doped with 2 at% of Pb. They found that, by Pb doping, thermoelectric performance of Mg$_2$Si can be greatly enhanced. The main reason is that the electrical conductivity σ increases enormously, leading to an increase of ZT, although the huge increase of σ in Pb-doped Mg$_2$Si is due to the formation of metallic Pb/Mg$_2$Pb phase at the grain boundaries. Note that Mg$_2$Si and Mg$_2$Pb have the same crystal structure type, but their electronic properties are quite different – the former is a semiconductor, while the latter is a metal. We here note that Mg$_2$Si and Mg$_2$Pb may form limited solid solutions (Mg$_2$Si$_{1-x}$Pb$_x$, 0 ≤ x ≤ 1), that means electronic structures of Mg$_2$Si$_{1-x}$Pb$_x$ solid solutions will vary with Pb/Si ratio, which is convenient for tuning their properties. To the best of our knowledge, there are few works related to thermoelectric properties of Mg$_2$Si$_{1-x}$Pb$_x$ solid solutions.

In the present work, we investigate structures and electronic properties of various Mg$_2$Si$_{1-x}$Pb$_x$ solid solutions using first-principles calculations. Firstly, we find that Mg$_2$Si$_{1-x}$Pb$_x$

^{a}International Center for Materials Discovery, School of Materials Science and Engineering, Northwestern Polytechnical University, Xi'an, Shaanxi 710072, P. R. China. E-mail: nwpufant@mail.nwpu.edu.cn

^{b}Science and Technology on Thermostructural Composite Materials Laboratory, School of Materials Science and Engineering, Northwestern Polytechnical University, Xi'an, Shaanxi 710072, P. R. China

^{c}Skolkovo Innovation Center, Skolkovo Institute of Science and Technology, Moscow 143026, Russia. E-mail: A.Oganov@skoltech.ru

^{d}Moscow Institute of Physics and Technology, 9 Institutskiy Lane, Dolgoprudny City, Moscow Region 141700, Russia

† Electronic supplementary information (ESI) available. See DOI: 10.1039/c8ra02436g
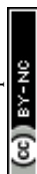
would become potential thermoelectric semiconductors in the range of $0 \leq x \leq 0.25$. We then investigate thermoelectric properties of $Mg_2Si_{1-x}Pb_x$ $(0 \leq x \leq 0.25)$ solid solutions, including Seebeck coefficient (α), electrical conductivity (σ), thermal conductivity (κ), and figure of merit (ZT). Compared with Mg_2Si, ZT of $Mg_2Si_{1-x}Pb_x$ solid solutions is improved. The highest ZT we found is 0.67 at 900 K of the composition $Mg_{64}Si_{30}Pb_2$.

2 Methods

Structure relaxations and total energy calculations were performed within density functional theory (DFT) using the projected augmented wave (PAW) method[29] as implemented in the VASP code.[30,31] We used the Perdew–Burke–Ernzerhof functional corresponding to the generalized gradient approximation (GGA-PBE).[32] The cutoff for the plane-wave basis was set to 600 eV and the Brillouin zone was sampled using Γ-centered uniform Monkhorst–Pack (MP) meshes[33] with the resolution of $2\pi \times 0.02$ Å^{-1} in all calculations. All geometries were fully optimized until the total energy difference between consecutive cycles was less than 10^{-8} eV and the maximum Hellmann–Feynman force was less than 10^{-3} eV Å^{-1}. To get more accurate band structures, hybrid functional (HSE06)[34,48] was used and spin–orbit coupling was neglected in our calculation.

For calculation of the interatomic force constants (IFCs) for each structure, a $2 \times 2 \times 2$ supercell was built and the real-space finite displacement method[35] was applied. The dynamical matrix was constructed based on the harmonic IFCs and phonon frequencies were obtained by diagonalizing the dynamical matrix using the PHONOPY package.[36]

Transport properties (Seebeck coefficient, electrical conductivity, and the electronic contribution to the thermal conductivity) were calculated in the framework of Boltzmann transport theory as implemented in the BoltzTrap code.[37] GGA-PBE was applied and the Brillouin zone was firstly sampled by a $6 \times 6 \times 6$ Monkhorst–Pack k-point mesh (20 points in the irreducible part of the Brillouin zone). Then a $41 \times 41 \times 41$ Monkhorst–Park k-point mesh (1771 in the IBZ) was used for the calculation of transport properties. After that, necessary derivatives were calculated on a FFT grid five times as dense. Moreover, for all structures, band gaps were set equal to the results of hybrid functional calculation in order to correct the well-known problem of GGA-PBE, which underestimate the band gap.

Lattice thermal conductivity of each structure was calculated based on a full iterative solution to the Boltzmann transport equation, as implemented in ShengBTE code.[38,39] Its main inputs are sets of second- and third-order interatomic force constants. For second-order IFCs, the results of PHONOPY calculation were directly used, while for third-order IFCs, a $2 \times 2 \times 2$ supercell was built and a finite-difference approach were employed. All interactions up to third-nearest neighbors were considered, noting that it is enough to get satisfactorily converged values. After harmonic and anharmonic IFCs were obtained, a $13 \times 13 \times 13$ q-point grid was used, meanwhile, both Born effective charges and dielectric tensors, which are required to determine the non-analytical part of the dynamical matrix, were involved in order to get the final thermal conductivity. At the same time, total Grüneisen parameter can be obtained as a weighted sum of the mode contributions.

To obtain absolute ZT values, electron relaxation time has to be calculated. Electron self-energy was calculated by combining QUANTUM ESPRESSO code[40] with EPW code.[41] Mg_2Si and Mg_2Pb primitive cell were used and the ground-state structures were computed within the local density approximation (LDA) of DFT as implemented in QUANTUM ESPRESSO code. Norm-conserving pseudopotentials were used to describe the core-valence interaction, and plane-wave kinetic energy cutoffs of 55 Ry and 70 Ry were used for the plane-wave basis set of Mg_2Si and Mg_2Pb, respectively. For both structures, the electronic states on $7 \times 7 \times 7$ k-point grid using DFT and the vibrational states on $7 \times 7 \times 7$ q-point grid using DFPT[42] were calculated. Then, the electron–phonon (e–ph) matrix elements were computed using these coarse grids. Later, in order to get the electron self-energy $\sum_{n,k}^{e-ph}$ associated with the electron–phonon interaction, where n is band number and k is k point in the Brillouin zone, these quantities are needed to be interpolated on significantly finer grids up to $50 \times 50 \times 50$ using an interpolation procedure based on Wannier functions implemented in the EPW code. After electron-phonon self-energy $\sum_{n,k}^{e-ph}$ was obtained, the e–ph scattering rate $\Gamma_{n,k}^{e-ph}$ was computed from the imaginary part of the self-energy as $\Gamma_{n,k}^{e-ph} = (2/\hbar)\text{Im}(\sum_{n,k}^{e-ph})$, and then the relaxation time defined as $\tau_{n,k} = (\Gamma_{n,k}^{e-ph})^{-1}$ was obtained by inverting the scattering rate. Such electron relaxation time calculation method proved to be effective in ref. 49, detailed calculation procedures can be found in ref. 50.

3 Results and discussion

3.1 Structures and electronic properties of $Mg_2Si_{1-x}Pb_x$ $(0 \leq x \leq 1)$

Previous study has shown that for good performance of a thermoelectric material, its bandgap should be in the range from 0.1 eV to 1 eV. Therefore, we need to investigate the composition range in which the bandgap can fulfil that condition.

Three $Mg_2Si_{1-x}Pb_x$ structures ($x = 0.25, 0.5, 0.75$) were built based on Mg_2Si conventional unit cell. In order to keep the ratio between Mg and Si/Pb constant, assuming that Pb can only substitute the site of Si and no interstitial. Since the symmetry of Mg_2Si is very high ($Fm\bar{3}m$) and all the Si atoms are symmetrically equivalent (with the same Wyckoff position 4a), we randomly chose the substitution sites at each specific composition. Some composition may have two or more different structures, such as $Mg_2Si_{0.5}Pb_{0.5}$, in this case, we selected the structure with the highest symmetry. We have optimized Mg_2Si, Mg_2Pb, and three constructed $Mg_2Si_{1-x}Pb_x$ structures very carefully at 0 K. Lattice parameters agree well with those reported before.[43,44] Mg_2Si and these three constructed $Mg_2Si_{1-x}Pb_x$ structures are shown in Fig. 1.

Band structures of these $Mg_2Si_{1-x}Pb_x$ structures were calculated using the hybrid functional HSE06. It shows that Mg_2Si has a bandgap of 0.66 eV, which is in good agreement with the experimental value 0.77 eV.[7] $Mg_2Si_{0.75}Pb_{0.25}$ is

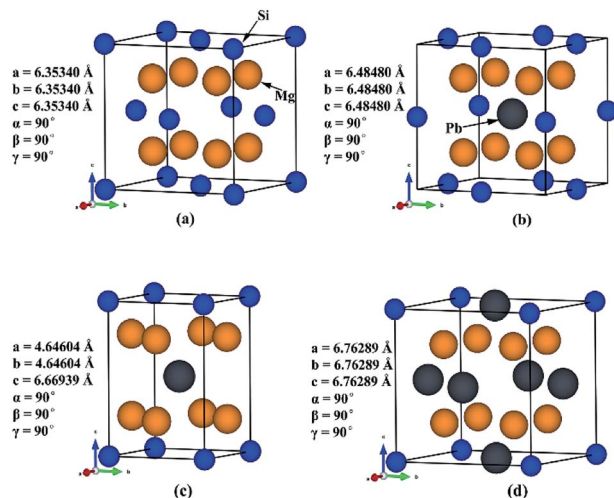Fig. 1 Crystal structures of (a) Mg_2Si; (b) $Mg_2Si_{0.75}Pb_{0.25}$; (c) $Mg_2Si_{0.5}Pb_{0.5}$; (d) $Mg_2Si_{0.25}Pb_{0.75}$.

a semiconductor with a narrow band gap of 0.08 eV, while the other two structures $Mg_2Si_{0.5}Pb_{0.5}$ and $Mg_2Si_{0.25}Pb_{0.75}$ are metals. Based on present calculations, we suggest that good thermoelectric performance of $Mg_2Si_{1-x}Pb_x$ compounds should be in the range of $0 \leq x \leq 0.25$. In the following sections, we focus on the investigation of thermoelectric properties of $Mg_2Si_{1-x}Pb_x$ solid solutions with $0 \leq x \leq 0.25$.

3.2 Two more $Mg_2Si_{1-x}Pb_x$ structures within $0 \leq x \leq 0.25$

To explore thermoelectric properties of $Mg_2Si_{1-x}Pb_x$ structures ($0 \leq x \leq 0.25$), we constructed two more $Mg_2Si_{1-x}Pb_x$ compositions ($Mg_{64}Si_{31}Pb$ and $Mg_{64}Si_{30}Pb_2$). First we built a $2 \times 2 \times 2$ supercell of Mg_2Si with 64 Mg atoms and 32 Si atoms, and then replaced one or two Si atoms with Pb atoms. Note that, in the case of $Mg_{64}Si_{30}Pb_2$, two Pb atoms placed at different distances have been carefully checked. We here use the method used by

Bilc et al.[45] and Hoang et al.,[46] the two Pb atoms were arranged as the first, second, third, fourth and fifth nearest neighbors with Pb–Pb distances in $\alpha/\sqrt{2}$, α, $\alpha\sqrt{3/2}$, $\alpha\sqrt{2}$, $\alpha\sqrt{3}$, respectively ($\alpha = 6.35340$ Å). We have optimized the constructed $Mg_{64}Si_{31}Pb$ and the five different $Mg_{64}Si_{30}Pb_2$ structures. These optimized structures are shown in Fig. 2.

We calculated formation energy E_f of a defect A in a bulk material defined as:[47]

$$E_f = E_{tot}(A) - E_{tot}(bulk) - \sum_i n_i \mu_i \tag{1}$$

Where $E_{tot}(A)$ is the total energy of supercell containing defect A and $E_{tot}(bulk)$ is the total energy of perfect supercell; μ_i is the chemical potential of atom i (host atoms or impurity atoms) and n_i represents the number of atoms of species i that have been added ($n_i > 0$) or removed ($n_i \leq 0$) to create the defect. What is more, μ_i is simply fixed to the total energy (per atom) of their standard metallic bulk structures, since the accurate values of the chemical potential are not relevant.

Fig. 3 shows the formation energies of Pb impurity pairs in Mg_2Si as a function of pair distance. The formation energy of the Pb pair at infinite distance is also given, which can be calculated by adding up the formation energy of an isolated Pb defect. It can be seen that the defect pair formation energies from 1st nearest distance to 5th nearest distance are very similar and the difference is within 0.01 eV, which suggests that all these states can coexist at high temperature, while they are all lower than that of Pb pair at infinite distance. Meanwhile, high positive values of the formation energy of Pb defect suggest that Pb does not tend to dissolve in Mg_2Si, which may be beneficial for lowering the lattice thermal conductivity due to scattering by precipitates. Furthermore, we used the structure having 2rd nearest distance Pb pair as representative of $Mg_{64}Si_{30}Pb_2$.

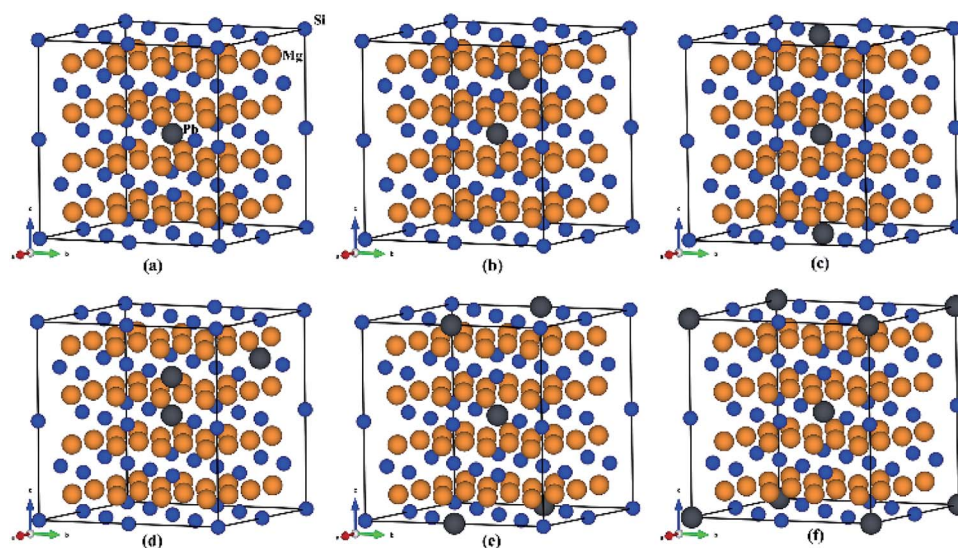We further investigated thermodynamical stability of these three $Mg_2Si_{1-x}Pb_x$ solid solutions: $Mg_{64}Si_{31}Pb$, $Mg_{64}Si_{30}Pb_2$ and

Fig. 2 Crystal structures for (a) $Mg_{64}Si_{31}Pb$; (b)–(f) correspond to the 1st, 2nd, 3rd, 4th, 5th nearest distance impurity pair of $Mg_{64}Si_{30}Pb_2$ structures respectively.
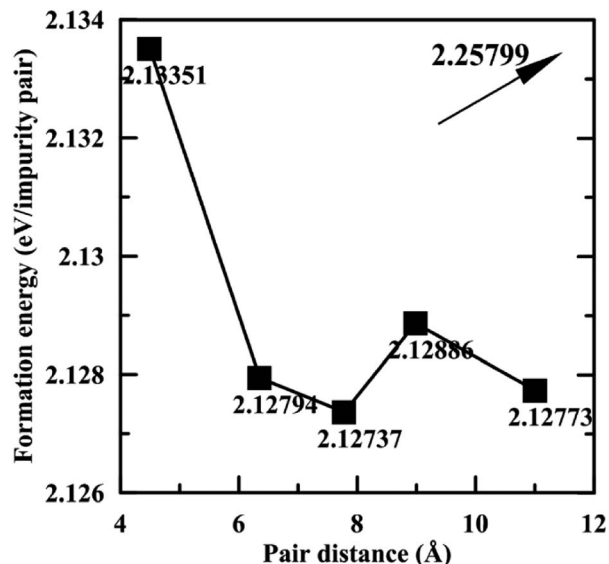
Fig. 3 Formation energies of Pb pair in Mg_2Si as a function of the pair distance. The value given with the arrow is the formation energy at infinite pair distance.

Mg_8Si_3Pb. Using Mg_2Si and Mg_2Pb as references, we calculated their formation enthalpies at 0 K and constructed the thermodynamic convex hull. As shown in Fig. 4, all these three structures possess positive formation enthalpies, indicating that they are metastable structures. However, all these three structures are within thermodynamically synthesize range because of their small positive formation enthalpies (less than 0.03 eV per atom).

3.3 Thermoelectric properties of $Mg_2Si_{1-x}Pb_x$ for $0 \leq x \leq 0.25$

Band structures are very important for understanding thermoelectric properties. We have calculated band structures of Mg_2Si, $Mg_{64}Si_{31}Pb$, $Mg_{64}Si_{30}Pb_2$ and Mg_8Si_3Pb using hybrid
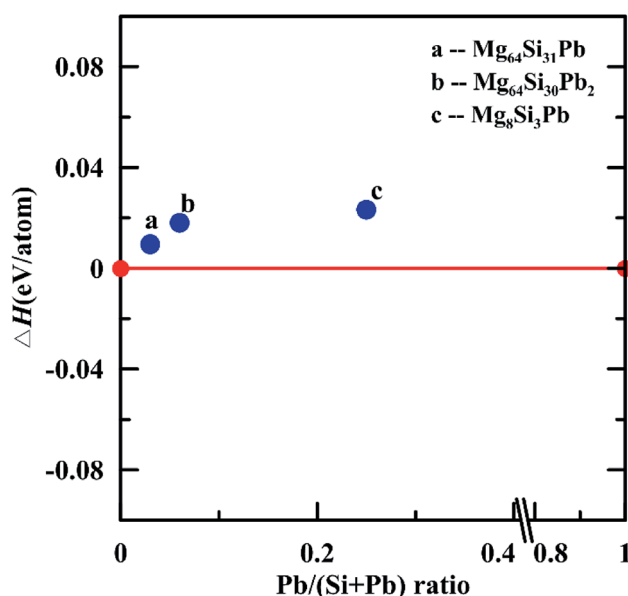
functional HSE06, as shown in Fig. 5 and S1 (ESI†). For all the four $Mg_2Si_{1-x}Pb_x$ structures, edges of the conduction bands and valence bands are asymmetric, and the conduction band minimum (CBM) and valence band maximum (VBM) occur at the gamma point in the k space. With the increasing of Pb concentration, band gap of $Mg_2Si_{1-x}Pb_x$ decreases.

We focus on the bands closest to Fermi level because they are important to determine the transport properties. Clearly, the three valence bands' positions in each $Mg_2Si_{1-x}Pb_x$ structures are lifted with the increasing of Pb concentration and their shapes and relative positions are almost unchanged. For the three conduction bands in each $Mg_2Si_{1-x}Pb_x$ structures, their situations are totally different (see Fig. S1, ESI†). In Mg_2Si, these three conduction bands separate at gamma point, and the second lowest band and the third lowest band lie above the CBM by ~8 meV and ~22 meV. As Pb concentration increases, the interaction between impurity states and host conduction-band states causes the above two bands to degenerate and the splitting between the CBM and those two bands is 5 meV, 10 meV and 576 meV, respectively, for $Mg_{64}Si_{31}Pb$, $Mg_{64}Si_{30}Pb_2$ and Mg_8Si_3Pb. Thus, by changing Pb concentration, it will not only lower the band gap but also change the distribution of the energy bands near the band-gap region.

We also calculated phonon dispersion curves for Mg_2Si, $Mg_{64}Si_{31}Pb$, $Mg_{64}Si_{30}Pb_2$ and Mg_8Si_3Pb. In this way, we confirmed their dynamical stability. As shown in Fig. 6, phonon dispersion curves of Mg_2Si, $Mg_{64}Si_{31}Pb$, $Mg_{64}Si_{30}Pb_2$, and Mg_8Si_3Pb have no imaginary frequencies. Being different from the phonon dispersion curves of Mg_2Si, the curves of $Mg_{64}Si_{31}Pb$, $Mg_{64}Si_{30}Pb_2$ and Mg_8Si_3Pb exhibit gaps between the longitudinal acoustic (LA) and transverse optic (TO) phonon branches. Usually, the low-frequency region of phonon dispersion curves is dominated by heavy atoms. When Pb is
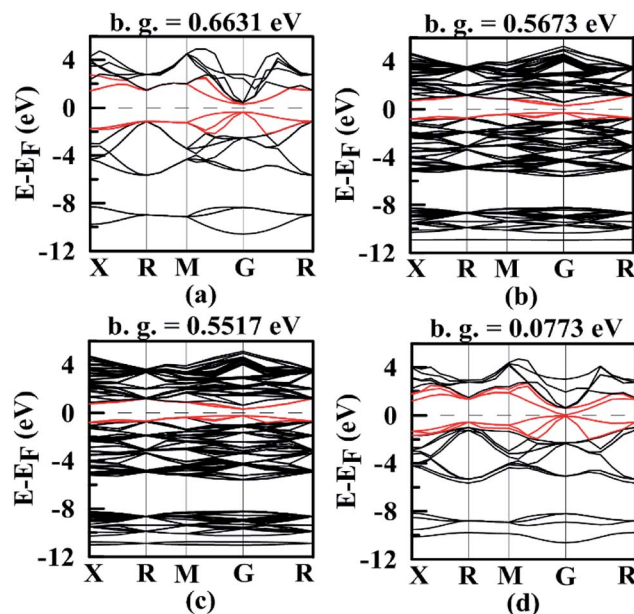

Fig. 4 Enthalpy of formation of three $Mg_2Si_{1-x}Pb_x$ solid solutions at 0 K.

Fig. 5 Band structures of (a) Mg_2Si; (b) $Mg_{64}Si_{31}Pb$; (c) $Mg_{64}Si_{30}Pb_2$; (d) Mg_8Si_3Pb. In each figure, the Fermi level E_F was shifted to zero and band gap value is displayed.

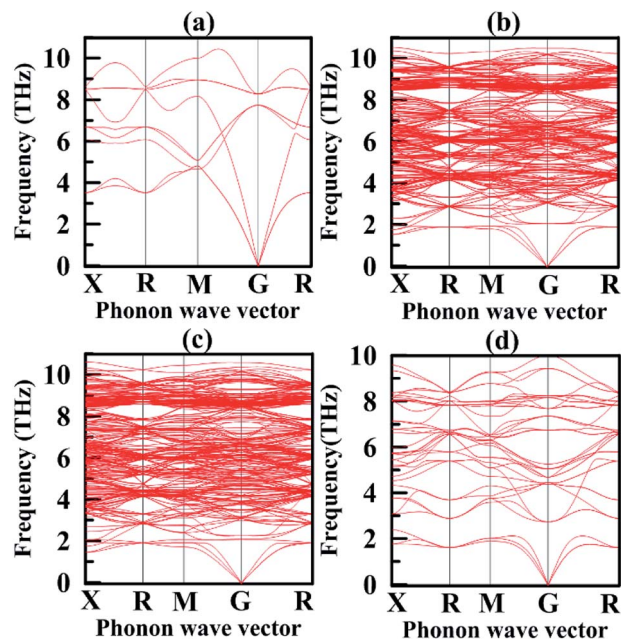**Fig. 6** Phonon dispersion curves of (a) Mg_2Si; (b) $Mg_{64}Si_{31}Pb$; (c) $Mg_{64}Si_{30}Pb_2$; (d) Mg_8Si_3Pb.

Fig. 7 Electron relaxation time in Mg_2Si and Mg_2Pb as a function of temperature.

introduced into Mg_2Si structure, three acoustic branches are lowered relative to those of Mg_2Si, which may suggest stronger anharmonicity.

We calculated thermoelectric properties for these four $Mg_2Si_{1-x}Pb_x$ structures including electron relaxation time τ, Seebeck coefficient α, electrical conductivity σ, thermal conductivity κ and figure of merit ZT. One important thing to mention is that is for α, σ and κ_e, which were calculated by BoltzTrap, we selected the values with chemical potential near the conduction band minimum, since it is known that Mg_2Si and its solid solutions usually are n-type thermoelectric materials.

Note that in most works, in order to get the absolute electrical conductivity calculated by BoltzTrap, electron relaxation time is either assumed to be constant or calculated by an empirical formula deduced from experimental values.[52] In this work, we find an effective non-empirical method[49,50] to calculate the electron relaxation time at different temperatures. This method may tend to overestimate the relaxation time at high temperatures because it only considers harmonic effects. A quantitative method to account for anharmonicity is still lacking. Fig. 7 shows temperature-dependent relaxation time of Mg_2Si and Mg_2Pb. For both materials, relaxation time decreases with temperature, but Mg_2Si shows stronger variation than Mg_2Pb. The relaxation time of Mg_2Si is an order of magnitude higher than that of Mg_2Pb in the entire temperature range, suggesting that the electron–phonon interaction is much stronger in Mg_2Pb than in Mg_2Si.

Fig. 8 shows temperature-dependent Seebeck coefficient (α) of these four $Mg_2Si_{1-x}Pb_x$ structures. For Mg_2Si, $Mg_{64}Si_{31}Pb$ and $Mg_{64}Si_{30}Pb_2$, Seebeck coefficients are all negative over the whole calculated temperature range and have similar values and tendency with temperature. In contrast, for Mg_8Si_3Pb, it shows a transition from n-type to p-type near 550 K. Our calculations
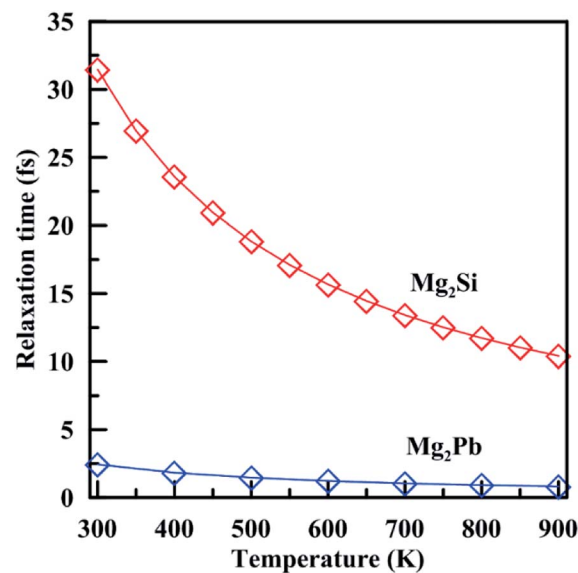
are in fair agreement with the experimental results whose carrier concentrations range from 1×10^{19} cm^{-3} to 1×10^{20} cm^{-3}, while have a discrepancy with nondoped Mg_2Si. The main reason for such a result is that we chose the values with chemical potential near the conduction band minimum, and the electron concentration near conduction band minimum is 1×10^{19} cm^{-3} $\sim$ 1×10^{20} cm^{-3} (this information can be read from the results of BoltzTrap calculation). Besides, the band gap we used in order to correct the results of GGA-PBE also has an evident influence on the results of transport coefficients. As can be seen in Fig. 8, we also show the results of Mg_2Si without band gap correction. There is clear difference induced by the correction, especially in the high temperature range.

Note that the electrical conductivity and electronic part of thermal conductivity calculated by BoltzTrap are in units of the
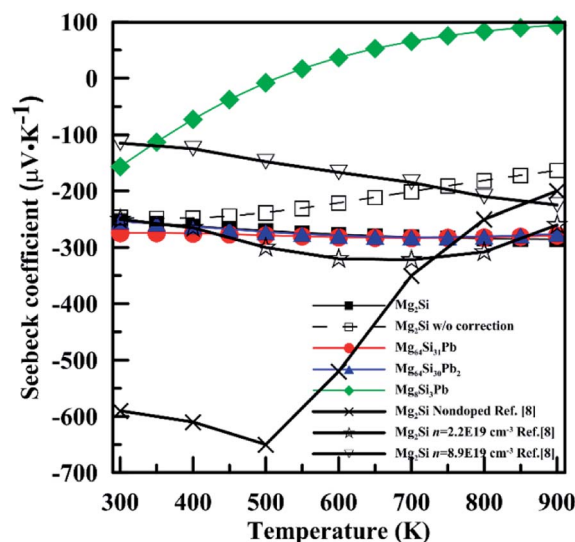

Fig. 8 Temperature dependence of Seebeck coefficient for n-type $Mg_2Si_{1-x}Pb_x$ solid solutions.

electron relaxation time; they are defined as σ/τ and κ_e/τ. To get σ and κ_e for all these four structures, we need the relaxation time of each structure. Calculation of the relaxation time is quite burdensome and time-consuming, especially for a large cell. Since we have obtained τ of Mg_2Si and Mg_2Pb, We assume that τ has a linear dependence with composition x,

$$\tau(Mg_2Si_{1-x}Pb_x) = (1-x)\tau(Mg_2Si) + x\tau(Mg_2Pb) \quad (2)$$

In practice, τ decreases more than linearly with composition x, and the calculated σ and κ_e can be used as upper bounds.

Fig. 9 shows the electrical conductivity (σ) of these four $Mg_2Si_{1-x}Pb_x$ structures as a function of temperature. σ of Mg_2Si matches well with those experimental results which have high electron concentration. Besides the reasons laid out in the discussion of the Seebeck coefficient, the relaxation time τ also has a great influence on the results of σ and κ_e. We can see these four structures have similar electrical conductivity, due to the similar carrier concentration near conduction band minimum.

Fig. 10 shows the temperature dependence of the total thermal conductivity ($\kappa = \kappa_e + \kappa_L$) and lattice thermal conductivity (κ_L) of these four $Mg_2Si_{1-x}Pb_x$ structures. κ_L of Mg_2Si obtained from our calculation matches well with the experiment value. For all four $Mg_2Pb_xSi_{1-x}$ structures, κ_L is proportional to T^{-1}, indicating phonon–phonon scattering as the key mechanism of thermal resistance. The introduction of Pb significantly lowers the lattice thermal conductivity of Mg_2Si: κ_L of Mg_2Si is 12.14 W m^{-1} K^{-1} at 300 K, while it is 4.18 W m^{-1} K^{-1}, 2.41 W m^{-1} K^{-1}, 3.76 W m^{-1} K^{-1} for $Mg_{64}Si_{31}Pb$, $Mg_{64}Si_{30}Pb_2$ and Mg_8Si_3Pb, respectively. This can be understood from the following two aspects: (1) introduction of Pb creates a large mass contrast throughout the crystal lattice, which will enhance phonon scattering and lead to a significant decrease of thermal conductivity; (2) according to the formula[51] used for evaluating κ_L:

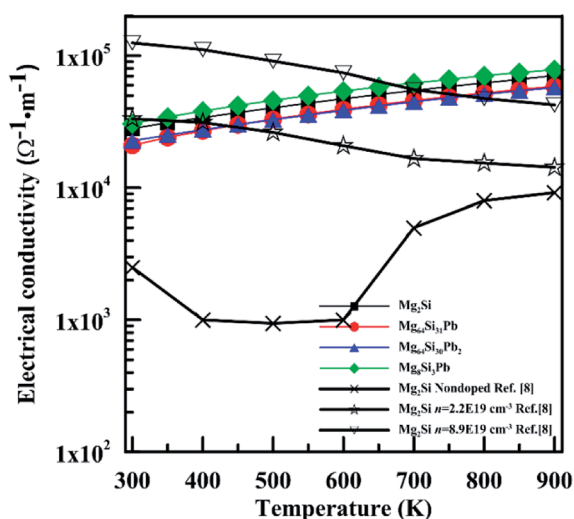$$\kappa_L \sim \frac{M\nu_m^3}{TV^{2/3}\gamma^2}\left(\frac{1}{N^{1/3}}\right) \quad (3)$$

in which M is the average mass, ν_m the mean speed of sound, γ the Grüneisen parameter, V the average volume per atom, and N the number of atoms per primitive unit cell. Because of the introduction of Pb, V and γ increase. We obtained thermodynamic Grüneisen parameters from 300 K to 850 K for these four structures, which is a result of ShengBTE calculation. As listed in Table 1.

Fig. 11 shows the temperature dependence of the figure of merit (ZT) of Pb-doped Mg_2Si compared with that of pristine Mg_2Si. It is obvious that ZT of $Mg_{64}Si_{31}Pb$ and $Mg_{64}Si_{30}Pb_2$ are improved compared with that of Mg_2Si, mainly due to the reduction of lattice thermal conductivity. The maximum ZT value of ~0.67 is found at 900 K for $Mg_{64}Si_{30}Pb_2$. In contrast, to Mg_8Si_3Pb, its ZT first decreases, then increases after 550 K, similar to what we saw for Seebeck coefficient.
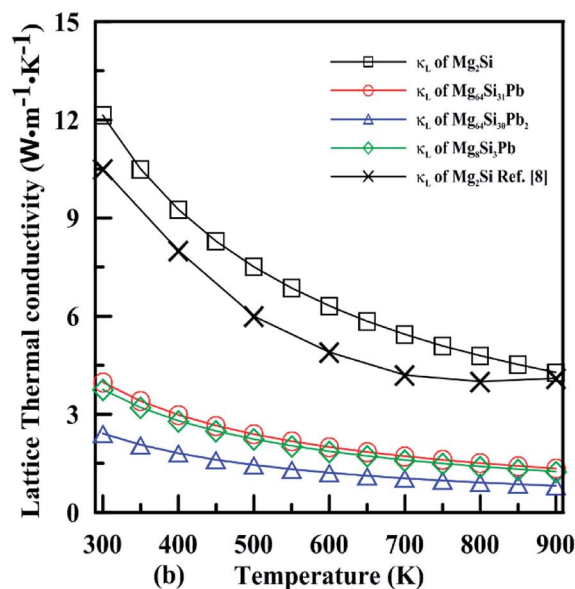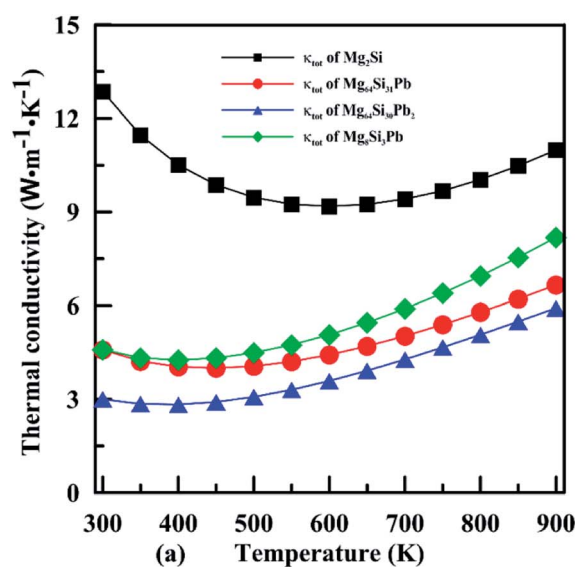

Fig. 10 Temperature dependence of the total thermal conductivity (a) and lattice thermal conductivity (b) for n-type $Mg_2Si_{1-x}Pb_x$ solid solutions.

Fig. 9 Temperature dependence of electrical conductivity for n-type $Mg_2Si_{1-x}Pb_x$ solid solutions.

Table 1 Thermodynamic Grüneisen parameters of $Mg_2Si_{1-x}Pb_x$ at different temperatures

Compound	300 K	350 K	400 K	450 K	500 K	550 K	600K	650 K	700 K	750 K	800 K	850 K
Mg_2Si	1.226	1.230	1.232	1.234	1.235	1.236	1.237	1.237	1.238	1.238	1.238	1.238
$Mg_{64}Si_{31}Pb$	1.255	1.259	1.261	1.263	1.264	1.265	1.266	1.267	1.267	1.267	1.268	1.268
$Mg_{64}Si_{30}Pb_2$	1.268	1.272	1.275	1.276	1.278	1.279	1.279	1.280	1.280	1.281	1.281	1.281
Mg_8Si_3Pb	1.365	1.368	1.370	1.371	1.372	1.372	1.373	1.373	1.374	1.374	1.374	1.374
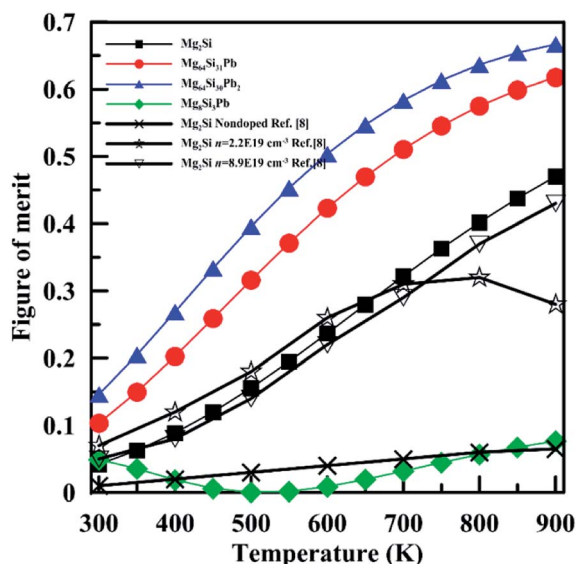
Fig. 11 Temperature dependence of figure of merit for n-type $Mg_2Si_{1-x}Pb_x$ solid solutions.

4 Conclusions

First-principles calculations combined with Boltzmann transport equation were used to study $Mg_2Si_{1-x}Pb_x$ solid solutions. The analysis of band structure features has shown that the composition x should be in the range of $0 \leq x \leq 0.25$ in order to be potential thermoelectric materials. Furthermore, four structures including Mg_2Si, $Mg_{64}Si_{31}Pb$, $Mg_{64}Si_{30}Pb_2$ and Mg_8Si_3Pb were studied in detail. Their band structures show that Pb impurities mainly influence the conduction bands near the Fermi level. As the Pb concentration increases, low-lying conduction band splits and goes towards the Fermi level. Then transport properties including electron relaxation time τ, Seebeck coefficient α, electrical conductivity σ, lattice thermal conductivity κ_L and thermoelectric figure of merit ZT were calculated between 300 K and 900 K. The computed τ indicates that the electron-phonon interaction is much stronger in Mg_2Pb than in Mg_2Si. Computed α and σ are close to experimental values with proper electron concentration, and κ_L matches well with experimental values. As for ZT, it shows that doping Pb can improve the ZT compared with that of Mg_2Si. $Mg_{64}Si_{30}Pb_2$ shows a maximum value of $ZT = 0.67$ at 900 K. The ZT value itself is not impressive, but it opens a way to optimize the thermoelectric properties of Mg_2Si. Our calculation shows that, it is the reduction of lattice thermal conductivity that mainly improves thermoelectric performance and it can still be improved by optimising the concentration of Pb. Most

importantly, this work shows that fully *ab initio* calculations of thermoelectric properties are possible, and provide accurate results.

Conflicts of interest

There are no conflicts of interest to declare.

Acknowledgements

Notes and references

1 D. M. Rowe, *Thermoelectrics handbook: macro to nano*, CRC press, 2005.
2 H. J. Goldsmid, *Introduction to thermoelectricity*, Springer Science & Business Media, 2009.
3 M. Fedorov, *J. Thermoelectr.*, 2009, **2**, 51–60.
4 M. I. Fedorov and G. N. Isachenko, *J. Appl. Phys.*, 2015, **54**, 07JA05.
5 A. Nozariasb, A. Agarwal, Z. A. Coutant, M. J. Hall, J. Liu, R. Liu, A. Malhotra, P. Norouzzadeh, M. C. Özturk, V. P. Ramesh, Y. Sargolzaeaval, F. Suarez and D. Vashaee, *J. Appl. Phys.*, 2017, **56**, 05DA04.
6 M. B. A. Bashir, S. Mohd Said, M. F. M. Sabri, D. A. Shnawah and M. H. Elsheikh, *Renewable Sustainable Energy Rev.*, 2014, **37**, 569–584.
7 V. Zaitsev, M. Fedorov, E. Gurieva, I. Eremin, P. Konstantinov, A. Y. Samunin and M. Vedernikov, *Proc. of 24th International Conference on Thermoelectrics (ICT 2005)*, Clemson, USA, 2005.
8 J.-i. Tani and H. Kido, *Physica B*, 2005, **364**, 218–224.
9 J.-i. Tani and H. Kido, *Intermetallics*, 2007, **15**, 1202–1207.
10 J.-i. Tani and H. Kido, *J. Alloys Compd.*, 2008, **466**, 335–340.
11 J.-Y. Jung and I.-H. Kim, *J. Electron. Mater.*, 2011, **40**, 1144–1149.
12 Q. S. Meng, W. H. Fan, R. X. Chen and Z. A. Munir, *J. Alloys Compd.*, 2011, **509**, 7922–7926.
13 D. Cederkrantz, N. Farahi, K. A. Borup, B. B. Iversen, M. Nygren and A. E. C. Palmqvist, *J. Appl. Phys.*, 2012, **111**, 023701.

14 N. Satyala and D. Vashaee, *Appl. Phys. Lett.*, 2012, **100**, 073107.

15 J.-H. Bahk, Z. Bian and A. Shakouri, *Phys. Rev. B*, 2014, **89**, 075204.

16 J.-H. Bahk, Z. Bian and A. Shakouri, *Phys. Rev. B*, 2013, **87**, 075204.

17 Y. Pei, H. Wang and G. Snyder, *Adv. Mater.*, 2012, **24**, 6125–6135.

18 H. Zhu, W. Sun, R. Armiento, P. Lazic and G. Ceder, *Appl. Phys. Lett.*, 2014, **104**, 082107.

19 J. P. Heremans, B. Wiendlocha and A. M. Chamoire, *Energy Environ. Sci.*, 2012, **5**, 5510–5530.

20 Y. Pei, X. Shi, A. LaLonde, H. Wang, L. Chen and G. J. Snyder, *Nature*, 2011, **473**, 66–69.

21 W. Liu, X. Tan, K. Yin, H. Liu, X. Tang, J. Shi, Q. Zhang and C. Uher, *Phys. Rev. Lett.*, 2012, **108**, 166601.

22 D. Pshenay-Severin and M. Fedorov, *Proc. of 25th International Conference on Thermoelectrics (ICT 2006)*, Vienna, Austria, 6-10 Aug, 2006.

23 G. Jiang, L. Chen, J. He, H. Gao, Z. Du, X. Zhao, T. M. Tritt and T. Zhu, *Intermetallics*, 2013, **32**, 312–317.

24 W. Liu, H. S. Kim, S. Chen, Q. Jie, B. Lv, M. Yao, Z. Ren, C. P. Opeil, S. Wilson, C.-W. Chu and Z. Ren, *Proc. Natl. Acad. Sci.*, 2015, **112**, 3269–3274.

25 Y. Noda, H. Kon, Y. Furukawa, N. Otsuka, I. A. Nishida and K. Masumoto, *Mater. Trans., JIM*, 1992, **33**, 845–850.

26 H. Ihou-Mouko, C. Mercier, J. Tobola, G. Pont and H. Scherrer, *J. Alloys Compd.*, 2011, **509**, 6503–6508.

27 J. Mao, H. S. Kim, J. Shuai, Z. Liu, R. He, U. Saparamadu, F. Tian, W. Liu and Z. Ren, *Acta Mater.*, 2016, **103**, 633–642.

28 S. Muthiah, J. Pulikkotil, A. Srivastava, A. Kumar, B. Pathak, A. Dhar and R. Budhani, *Appl. Phys. Lett.*, 2013, **103**, 053901.

29 G. Kresse and D. Joubert, *Phys. Rev. B*, 1999, **59**, 1758–1775.

30 G. Kresse and J. Furthmüller, *Phys. Rev. B*, 1996, **54**, 11169–11186.

31 G. Kresse and J. Furthmüller, *Comput. Mater. Sci.*, 1996, **6**, 15–50.

32 J. P. Perdew, K. Burke and M. Ernzerhof, *Phys. Rev. Lett.*, 1996, **77**, 3865–3868.

33 H. J. Monkhorst and J. D. Pack, *Phys. Rev. B*, 1976, **13**, 5188–5192.

34 J. Heyd and G. E. Scuseria, *J. Chem. Phys.*, 2003, **118**, 8207–8215.

35 K. Esfarjani and H. T. Stokes, *Phys. Rev. B*, 2008, **77**, 144112.

36 A. Togo, F. Oba and I. Tanaka, *Phys. Rev. B*, 2008, **78**, 134106.

37 G. K. Madsen and D. J. Singh, *Comput. Phys. Commun.*, 2006, **175**, 67–71.

38 W. Li, L. Lindsay, D. A. Broido, D. A. Stewart and N. Mingo, *Phys. Rev. B*, 2012, **86**, 174307.

39 W. Li, J. Carrete, N. A. Katcho and N. Mingo, *Comput. Phys. Commun.*, 2014, **185**, 1747–1758.

40 G. Paolo, B. Stefano, B. Nicola, C. Matteo, C. Roberto, C. Carlo, C. Davide, L. C. Guido, C. Matteo, D. Ismaila, C. Andrea Dal, G. Stefano de, F. Stefano, F. Guido, G. Ralph, G. Uwe, G. Christos, K. Anton, L. Michele, M.-S. Layla, M. Nicola, M. Francesco, M. Riccardo, P. Stefano, P. Alfredo, P. Lorenzo, S. Carlo, S. Sandro, S. Gabriele, P. S. Ari, S. Alexander, U. Paolo and M. W. Renata, *J. Phys.: Condens. Matter*, 2009, **21**, 395502.

41 J. Noffsinger, F. Giustino, B. D. Malone, C.-H. Park, S. G. Louie and M. L. Cohen, *Comput. Phys. Commun.*, 2010, **181**, 2140–2148.

42 S. Baroni, S. de Gironcoli, A. Dal Corso and P. Giannozzi, *Rev. Mod. Phys.*, 2001, **73**, 515–562.

43 J. Bourgeois, J. Tobola, B. Wiendlocha, L. Chaput, P. Zwolenski, D. Berthebaud, F. Gascoin, Q. Recour and H. Scherrer, *Funct. Mater. Lett.*, 2013, **6**, 1340005.

44 K. Kutorasinski, B. Wiendlocha, J. Tobola and S. Kaprzyk, *Phys. Rev. B*, 2014, **89**, 115205.

45 D. Bilc, S. D. Mahanti, E. Quarez, K.-F. Hsu, R. Pcionek and M. G. Kanatzidis, *Phys. Rev. Lett.*, 2004, **93**, 146403.

46 K. Hoang, S. D. Mahanti and M. G. Kanatzidis, *Phys. Rev. B*, 2010, **81**, 115106.

47 C. G. Van de Walle and J. Neugebauer, *J. Appl. Phys.*, 2004, **95**, 3851–3879.

48 G. Kresse, M. Marsman and J. Furthmüller, *Si bandstructure*, http://cms.mpi.univie.ac.at/wiki/index.php/Si_bandstructure, (accessed 7 Oct, 2017).

49 M. Bernardi, D. Vigil-Fowler, C. S. Ong, J. B. Neaton and S. G. Louie, *Proc. Natl. Acad. Sci.*, 2015, **112**, 5291–5296.

50 S. Poncé, R. Margine, C. Verdi and F. Giustino, *B-doped diamond*, http://epw.org.uk/Documentation/B-dopedDiamond, (accessed 7 Oct, 2017).

51 W. G. Zeier, A. Zevalkink, Z. M. Gibbs, G. Hautier, M. G. Kanatzidis and G. J. Snyder, *Angew. Chem., Int. Ed.*, 2016, **55**, 6826–6841.

52 J. Sun and D. J. Singh, *Phys. Rev. Appl.*, 2016, **5**, 024006.

53 J.-J. Wang, A. Hermann, X.-Y. Kuang, Y.-Y. Jin, C. Lu, C.-Z. Zhang, M. Ju, M.-T. Si and T. Iitaka, *RSC Adv.*, 2015, **5**, 53497–53503.